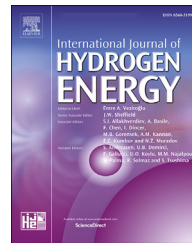




ELSEVIER

Available online at www.sciencedirect.com

ScienceDirect

journal homepage: www.elsevier.com/locate/he

Structural peculiarities of $\text{La}_2\text{Ge}_{1-x}\text{Cr}_x\text{MgO}_{6-\delta}$ ($0 < x \leq 0.5$): a superior oxide-ion electrolyte for low-temperature solid-oxide fuel cells

C.A. López ^{a,b}, Preetam Singh ^c, R. Martínez-Coronado ^a, J.A. Alonso ^{a,*}^a Instituto de Ciencia de Materiales de Madrid, CSIC, Cantoblanco 28049 Madrid, Spain^b INTEQUI, (UNSL-CONICET) and Facultad de Química, Bioquímica y Farmacia, UNSL, Almirante Brown 1455, 5700, San Luis, Argentina^c Department of Ceramic Engineering, IIT-BHU Varanasi, Uttar Pradesh 221005, India

HIGHLIGHTS

- A novel series of electrolyte materials over-perform in electrolyte-supported SOFC cells.
- Ge-containing perovskites where both Ge^{4+} and Cr^{3+} ions can exhibit octahedral and tetrahedral oxygen coordination.
- Oxygen vacancies generated by Cr doping favor oxygen diffusion across the crystal structure.
- A neutron powder diffraction (NPD) study of the perovskite matrix unveils the oxygen diffusion paths.
- The power density of test cells at 600 °C is ~600 mW cm⁻², a threefold increase compared with LSGM electrolyte.

ARTICLE INFO

Article history:

Received 18 October 2022

Received in revised form

13 December 2022

Accepted 15 December 2022

Available online 3 January 2023

Keywords:

Solid-oxide electrolyte

Defect perovskite structure

Neutron diffraction

Oxygen vacancies

ABSTRACT

The double perovskite $\text{La}_2\text{MgGeO}_6$ has been modified by substitution of Ge by Cr to introduce oxygen vacancies. A specimen of composition $\text{La}_2\text{Ge}_{0.55}\text{Cr}_{0.45}\text{MgO}_6$ has been studied by neutron diffraction, in the 300–873 K temperature range. The perovskite structure can be defined in the rhombohedral R3 space group. At 295 K, the unit-cell parameters are $a = 5.5115 (2)$, $c = 13.3485 (7)$ Å and $V = 351.16 (3)$ Å³. This double perovskite exhibits two distinct crystallographic sites for Mg and (Cr,Ge), statistically distributed at the octahedral sites. It presents a conspicuous deficiency at O1 sites, accounting for the excellent ionic conduction properties. The Bond-Valence Energy Landscape (BVEL) map at 873 K shows that oxygen atoms present a higher mobility around the (Ge/Cr)_O octahedra than the MgO_6 ones; therefore, the “bottleneck” points for oxygen mobility are placed between the (Ge/Cr)_O octahedra around the La^{3+} and Mg^{2+} cations. The dark-red samples prepared in air show evidence of oxidation of some Cr^{3+} to Cr^{4+} to give a polaronic component to a conductivity of 10^{-2} Scm⁻¹ at 300 °C for $\text{La}_2\text{Ge}_{0.5}\text{Cr}_{0.5}\text{MgO}_{6-\delta}$; Arrhenius plots of conductivity obtained on cooling from 900 °C to 25 °C in air give an activation energy of ~0.25 eV. The fuel-cell performance at 600 °C gave a power density of 606 mW cm⁻², a threefold increase over the output compared with LSGM electrolyte.

© 2023 The Authors. Published by Elsevier Ltd on behalf of Hydrogen Energy Publications

LLC. This is an open access article under the CC BY-NC-ND license (<http://creativecommons.org/licenses/by-nc-nd/4.0/>).

* Corresponding author.

E-mail address: ja.alonso@icmm.csic.es (J.A. Alonso).<https://doi.org/10.1016/j.ijhydene.2022.12.193>

Introduction

Solid-oxide fuel cells (SOFC) are electrochemical devices that convert the chemical energy of a fuel into electricity in a clean and reversible way [1]. They offer a multi-fuel capability; not only hydrogen or carbon monoxide, but also various hydrocarbon species can be made as fuel by the introduction of internal or simple external fuel reforming reactions [2–7]. SOFCs rely on a solid-oxide electrolyte having a high oxide-ion conductivity σ_o enabling the chemical transport of O^{2-} ions from the cathode to the anode, where they recombine with the fuel [8]. This reversible technology affords working in SOEC (solid-oxide electrolyzer cell) mode [9–12], converting electrical energy from solar, wind and nuclear energy [13] and generating H_2 or methanol from steam and/or CO_2 [14].

The key technical issue that has limited the development of this technology is the high operation temperatures [15], $T_{op} \sim 1000$ °C, which results in higher system costs and performance-degradation rates, as well as slow start-up and shut-down times, the latter dramatically limiting its applicability to portable power and transportation markets [16–18]. Addressing the increasing polarization losses associated with electrolyte conduction and electrode reaction kinetics as T_{op} is lowered are the key issues limiting lower temperature operation [19,20] and have been the focus of many groups over the past few decades [21–38]. The entire SOFC material set is dependent on the selection of the electrolyte and its chemical and thermo-mechanical stability with respect to the electrodes. The vast majority of SOFCs use a zirconia-based electrolyte, typically yttrium-stabilized zirconia (YSZ) [39,40] or gadolinium-stabilized ceria (GDC) [41–43], because of its superior stability with respect to the catalytic electrolyte. Although a good oxygen-ion conductor above 800 °C, YSZ is far from having the highest conductivity [29].

The most common oxide-ion electrolytes have an oxygen-deficient, cubic fluorite or perovskite structure with oxygen transport via oxygen vacancies. However, the apatite, scheelite, Ruddlesden–Popper, and mayenite structures provide examples where oxide-ion transport is by interstitial oxide ions [22–37]. Whereas the perovskite $La_{0.8}Sr_{0.2}Ga_{0.83}Mg_{0.17}O_{2.81}$ (LSGM) is an example of an oxygen-vacancy conductor [23,24,44], the melilite structure of the competitive phase $La_{1+x}Sr_{1-x}Ga_3O_{7+x}$ contains mobile interstitial oxide ions [26,27].

However, superior oxide-ion conductivity ($\sigma_o > 10^{-2}$ Scm⁻¹, $T < 500$ °C) can be realized if the vacancy movement can happen freely in all three dimensions. A new oxide-ion electrolyte based on the parent double perovskite La_2GeMgO_6 phase [45] has been identified; it is the only Ge-containing perovskite existing at ambient temperature and pressure. The double perovskite La_2GeMgO_6 phase crystallizes in a hexagonal cell (R3 space group) with ordering of Ge and Mg octahedra. The substitution of M^{3+} cations for Ge^{4+} introduces oxygen vacancies that can diffuse in all three directions with a low activation energy by an oxygen-vacancy mechanism, because both the Mg^{2+} and Ge^{4+} cations are stable in both tetrahedral and octahedral oxygen coordination. Indeed, we obtained superior oxide-ion conductivity ($\sigma_o > 10^{-2}$ Scm⁻¹, $T \geq 300$ °C) by substitution of Cr^{3+} for the Ge^{4+} ion in the

$La_2Ge_{1-x}Cr_xMgO_{6-\delta}$ ($0 < x \leq 0.5$) series; the Cr^{3+} ions have a strong octahedral site preference and prevent the ordering of vacancies.

On the other hand, neutron powder diffraction (NPD) is a powerful tool for the determination of subtle structural details, especially in oxides [46–50]. Here we provide with precise structural characterization from (NPD) data of a selected member of the series of composition $La_2Ge_{0.55}Cr_{0.45}MgO_{6-\delta}$, including a visualization of the oxide-ions diffusion path, which unveils interesting peculiarities of the different octahedral coordination environments.

Experimental

$La_2Ge_{1-x}Cr_xMgO_{6-\delta}$ ($0 < x \leq 0.5$) samples were synthesized by solid-state reaction from stoichiometric amounts of La_2O_3 , GeO_2 , Cr_2O_3 and MgO powders, ground and heated for 20 h at 1350 °C. The samples were obtained by slow furnace cooling to room temperature. For conductivity measurements, the resulting powders were made into pellets (typically ~0.2 cm in thickness and ~1 cm in diameter) by pressing the powder with 1 wt % of polyvinyl butyral (PVB) at 5 GPa and firing for 20 h at 1400 °C.

The phase purity of the compounds was confirmed by powder X-ray diffraction (XRD) with a Philips X'pert diffractometer (Cu K α radiation, $\lambda = 1.5418$ Å) in Bragg-Brentano reflection geometry. Neutron powder diffraction (NPD) patterns were collected at 298, 573 and 873 K and for a selected composition $La_2Ge_{0.55}Cr_{0.45}MgO_{6-\delta}$ at the HRPT diffractometer of the SINQ spallation source (PSI, Paul Scherrer Institute, Villigen, Switzerland). A Rietveld structure refinement was carried out with the Fullprof program. A pseudo-Voigt function was chosen to generate the line shape of the diffraction peaks. The following parameters were refined in the final runs: scale factor, background coefficients, zero-point error, pseudo-Voigt peak profiles corrected for asymmetry parameters, unit-cell parameters and isotropic thermal factors. The scattering factors for La, Ge, Cr, Mg and O were 8.24, 8.185, 3.635, 5.375 and 5.803 fm, respectively.

Single test cells were fabricated by an electrolyte-supported technique. A 300-μm-thick $La_2Ge_{0.5}Cr_{0.5}MgO_{6-\delta}$ (LGCM) disk was used as the electrolyte, commercial $NiO-Ce0.8Gd0.2O2-\delta$ (GDC) was used as the anode and $SrCo0.8Fe0.2O3$ (SCFO) was the cathode. NiO -GDC and SCFO were made into a paste with a commercial binder (V-006, Heraeus). SCFO was screen printed onto one side of the disk and fired at 1100 °C in air for 1 h. NiO -GDC was finally screen printed onto the other side of the disk and fired at 1100 °C in 5% H_2/N_2 for 1 h. The working electrode area of the cell was 0.24 cm² (0.6 × 0.4 cm). Pt gauze with a small amount of Pt paste in separate dots was used as current collector at both the anodic and the cathodic sides for ensuring electrical contact. The cells were tested in a vertical tubular furnace with air directly supplied to the cathode surface and hydrogen to the anode surface. The performance measurements were carried out at 550, 600, and 650 °C. The fuel-cell tests were performed with an AUTOLAB 302 N Potentiostat/Galvanostat by changing the voltage of the cell from the OCV (“Open Circuit Voltage”) to 0.1 V with steps of 0.050 V, holding 40 s at each

step. Current density was calculated by the recorded current flux through the effective area of the cell (0.24 cm^2).

Results and discussion

As synthesized $\text{La}_2\text{Ge}_{1-x}\text{Cr}_x\text{MgO}_{6-\delta}$ ($x = 0.2, 0.3, 0.35, 0.4, 0.45, 0.5$) powders are dark red in color; however, undoped $\text{La}_2\text{GeMgO}_6$ powder is off-white in color. The XRD patterns of all the compounds of the series are shown in Fig. S1 at the Supporting Information. Rietveld refinement of the XRD profile of nominal $\text{La}_2\text{Ge}_{0.5}\text{Cr}_{0.5}\text{MgO}_{6-\delta}$ is illustrated in Fig. 1, exhibiting an excellent agreement with the profile generated in the space group R3.

A NPD investigation was essential to unveil subtle details of this double perovskite, since neutrons are sensitive to oxygen positions, yielding information on the octahedral tilting and the presence of oxygen vacancies. This was studied in a selected sample with $\text{La}_2\text{Ge}_{0.55}\text{Cr}_{0.45}\text{MgO}_{6-\delta}$ composition. The crystal structure was defined according to the model reported for the parent $\text{La}_2\text{GeMgO}_6^{45}$. In the R3 (No 146) space group, hexagonal description, the two La sites, Ge and Mg occupy the $3a$ ($0,0,z$) Wyckoff sites, whereas the two types of O are located at $9b$ (x,y,z) sites. Cr is statistically distributed at Ge positions. A conspicuous oxygen deficiency was identified at O1 atoms. Table 1 summarizes the main structural parameters after the Rietveld refinement of the structure. Minor impurities of MgO , La_2O_3 and La(OH)_3 were also included in the refinement. Fig. 2a shows the quality of the neutron fit, and Fig. 2b illustrates the crystal structure, highlighting the alternation of $(\text{Ge,Cr})\text{O}_6$ and MgO_6 octahedra in the three directions.

The NPD patterns collected above room temperature ($T = 573, 873\text{ K}$) could be refined in the same space group R3, showing no evidence of phase transitions or degradation of the samples. The Supplementary Information includes Tables S2 and S3, and Figure S2a and S2b with the atomic parameters and Rietveld plots at $T = 573$ and 873 K , respectively. Fig. 3

displays the thermal evolution of the unit-cell volume and the a and c parameters; a monotonous expansion is observed as the sample is warmed up, as expected.

On the other hand, in order to evaluate the oxygen mobility of this ionic conductor, the BondValence Energy Landscape (BVEL) was calculated. Starting from the determined atomic parameters, this methodology enables obtaining the most probable oxygen diffusion pathway across the lattice based upon bond-valence considerations [51]. Fig. 4 shows the obtained BVEL map at 873 K . In a more detailed analysis, it is possible to observe that the oxygen atoms present a higher mobility around the $(\text{Ge/Cr})\text{O}_6$ octahedra than the MgO_6 ones, as shown in Fig. 5. Thus, the “bottleneck” points for oxygen mobility are placed between the $(\text{Ge/Cr})\text{O}_6$ octahedra around the La^{3+} and Mg^{2+} cations. These points with high electrostatic energy for the O^{2-} diffusion can be quantified from BVEL through the percolation energies, tabulated in Table S4 at the SI document. Although these values cannot be related to the band gap energy obtained from ab-initio calculations or other experimental studies, they allow establishing some predictions about the ionic conductivity. For example, it is possible to note that at higher temperatures the mobility within the a - b plane is preferable over that along c direction. By contrast, at room temperature there are not substantial differences in percolation energies, suggesting that the O^{2-} mobility is energetically isotropic in the three directions. These are in agreement with the thermal evolution of the unit-cell parameters, which show a higher increase along c than in the a - b direction (see Fig. 3).

Transport properties and thermal stability

Owing to the absence of an oxide-ion vacancy, the parent $\text{La}_2\text{GeMgO}_6$ perovskite does not show any measurable oxide-ion conductivity even at higher temperatures. The oxide-ion conductivity (σ_o vs T ($^\circ\text{C}$)) and Arrhenius plot ($\ln(\sigma_o)$ vs $1000/T$ (K^{-1})) for different $\text{La}_2\text{Ge}_{1-x}\text{Cr}_x\text{MgO}_{6-\delta}$ ($0 < x \leq 0.5$)

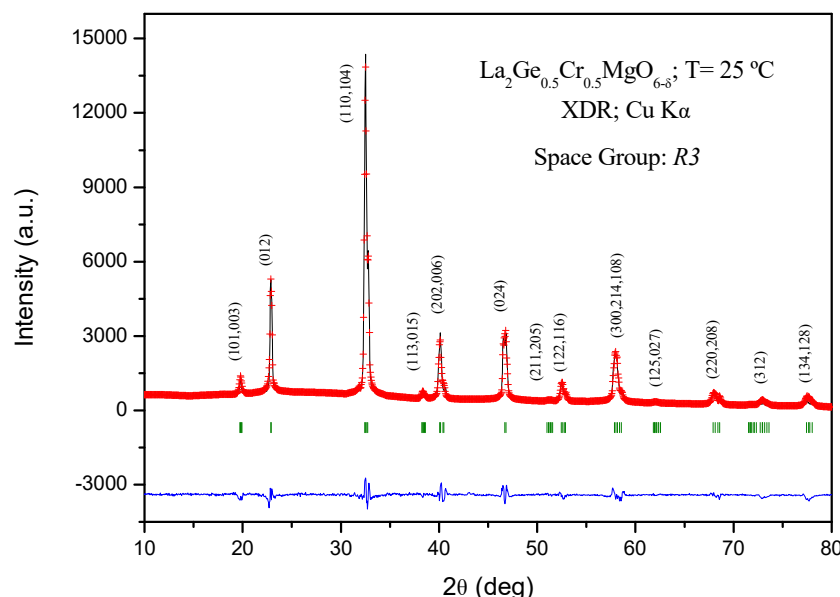


Fig. 1 – XRD Rietveld plot for $\text{La}_2\text{Ge}_{0.5}\text{Cr}_{0.5}\text{MgO}_{6-\delta}$, defined in the R3 space group.

**Table 1 – Crystallographic data for $\text{La}_2\text{Ge}_{0.55}\text{Cr}_{0.45}\text{MgO}_6$ phase in Rhombohedral R3 space group from NPD at 300 K
 $a = 5.5115(2)$ Å, $c = 13.3485(7)$ Å and $V = 351.16(3)$ Å³.**

	x	y	Z	$U_{\text{iso}}^*/U_{\text{eq}}$	Occ. (<1)
La1	0.00000	0.00000	0.2473 (5)	0.0155 (11)*	
La2	0.00000	0.00000	0.7527 (5)	0.0155 (11)*	
Ge	0.00000	0.00000	0.5046 (18)	0.016 (2)*	0.55
Cr	0.00000	0.00000	0.5046 (18)	0.016 (2)*	0.45
Mg	0.00000	0.00000	0.00000	0.007 (2)*	
O1	0.1042 (17)	0.332 (3)	0.0852 (12)	0.017 (3)*	0.925 (2)
O2	0.1252 (14)	0.8022 (15)	0.5998 (6)	0.0013 (10)*	

$R_p = 6.47\%$, $R_{wp} = 8.62\%$, $\chi^2 = 6.52$, $R_{\text{Bragg}} = 6.26\%$
Impurities: MgO (0.82%) and La_2O_3 (2.48%)

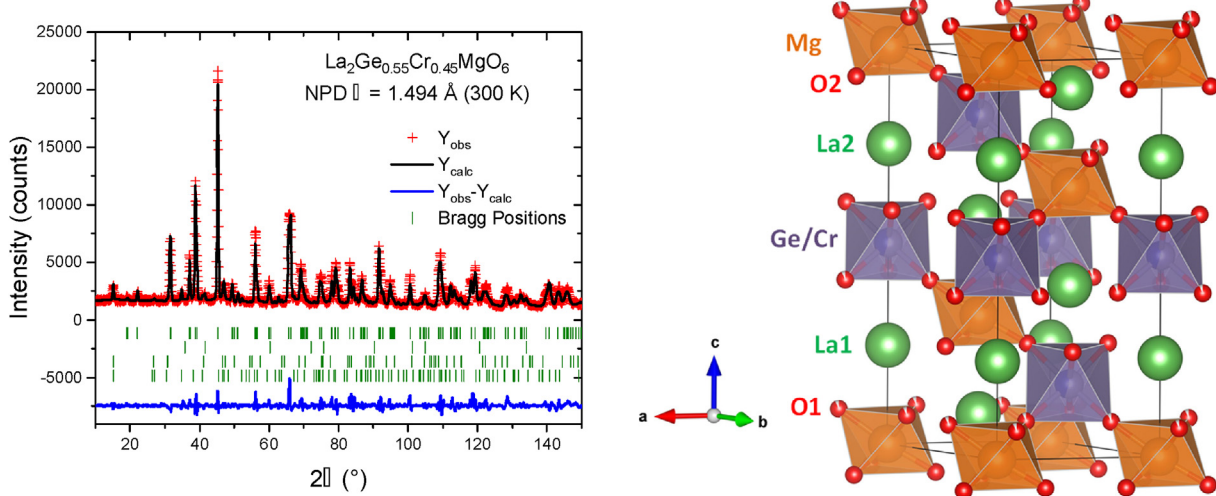


Fig. 2 – a) Rietveld plot from NPD data. The four series of Bragg reflections (green ticks) correspond to the main R3 perovskite phase, and minor impurities of MgO , La_2O_3 and $\text{La}(\text{OH})_3$. b) View of the crystal structure of $\text{La}_2\text{Ge}_{0.55}\text{Cr}_{0.45}\text{MgO}_{6-\delta}$, illustrating the alternation of MgO_6 and $(\text{Ge}/\text{Cr})\text{O}_6$ octahedra. (For interpretation of the references to colour in this figure legend, the reader is referred to the Web version of this article.)

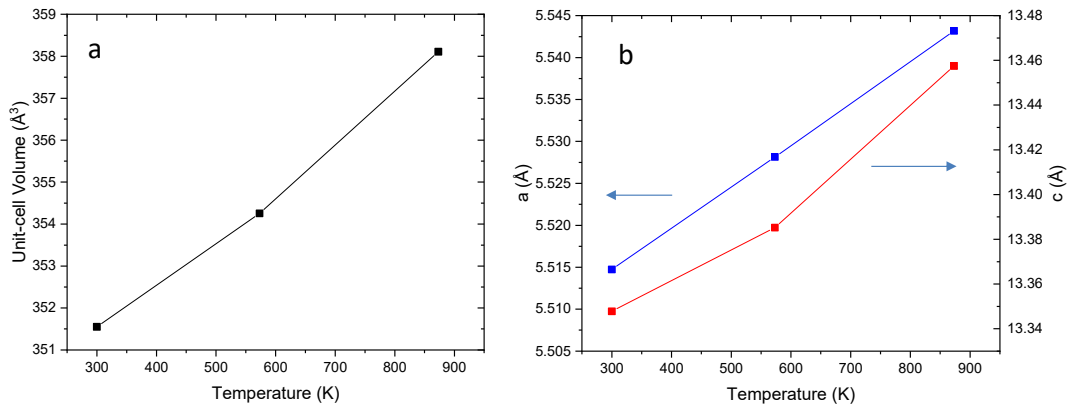


Fig. 3 – a) Unit-cell volume and b) unit-cell parameters thermal variation for $\text{La}_2\text{Ge}_{0.55}\text{Cr}_{0.45}\text{MgO}_6$.

compositions are shown in Fig. 6(a–b). An additional plot of the conductivity measured in different atmospheres is shown in Fig S3. Almost the same oxide-ion conductivity was observed for the $\text{La}_2\text{Ge}_{0.5}\text{Cr}_{0.5}\text{MgO}_{6-\delta}$ sample in all environments, which indicates the presence of a minimal electronic conductivity in the sample. The conductivity measurement

was done by cooling the sample from 800 °C to 25 °C, which also rules out the presence of protons in the sample for any protonic conductivity. The conductivities (σ_a) are thus assumed to be oxide-ion only; the values determined at different temperatures and the activation energies for the different compositions of $\text{La}_2\text{Ge}_{1-x}\text{Cr}_x\text{MgO}_{6-\delta}$ are given in Table

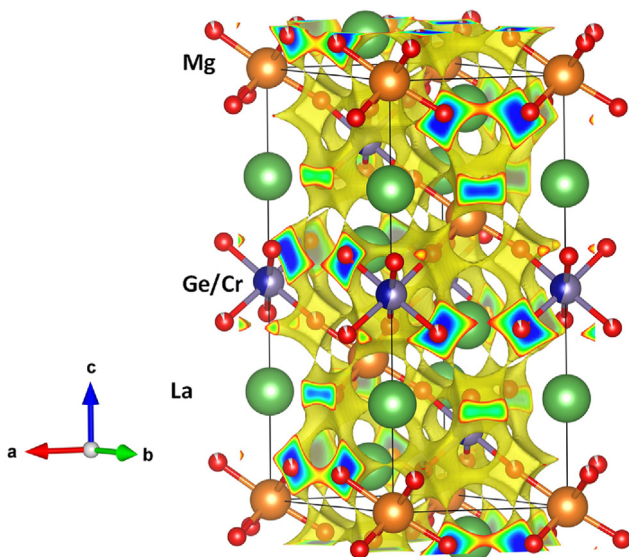


Fig. 4 – Oxygen diffusion pathways across the $\text{La}_2\text{Ge}_{0.5}\text{Cr}_{0.45}\text{MgO}_6$ structure at 873 K.

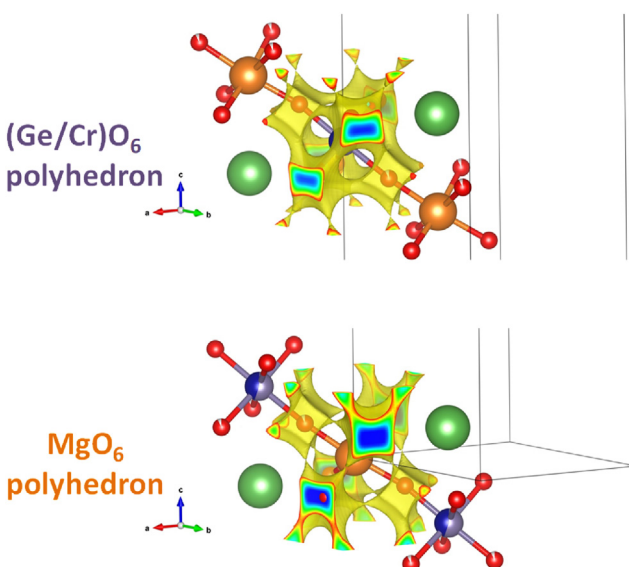


Fig. 5 – Percolation pathways for O diffusion around the $(\text{Ge/Cr})\text{O}_6$ and MgO_6 octahedra.

S5 (Supporting Information). The Arrhenius plot is almost linear in the temperature range of 25–900 °C, which indicates a low activation energy (Table S5) of the mobile species (~0.25 eV) and the apparent absence of condensation of mobile oxide-ion vacancies above 200 °C. The oxidation of some Cr^{3+} to Cr^{4+} introduces a polaronic conduction that contributes little to the low-temperature conductivity. The oxide-ion conductivity increases with increasing amount of Cr^{3+} substitution for Ge^{4+} (x), which increments the oxide-ion vacancy concentration. The maximum oxide-ion conductivity of $1.37 \times 10^{-2} \text{ Scm}^{-1}$ at $T_{\text{op}} = 300$ °C was observed for $x = 0.5$, $\text{La}_2\text{Ge}_{0.5}\text{Cr}_{0.5}\text{MgO}_6$ (Table S5). A similar conductivity was observed for other well-known oxide-ion conductors only at much higher temperatures, i.e. for YSZ ($\text{Zr}_{1-x}\text{Y}_x\text{O}_{2-0.5x}$ ($x = 0.08$)

at $T \geq 700$ °C, LSGM ($\text{La}_{0.8}\text{Sr}_{0.2}\text{Ga}_{0.83}\text{Mg}_{0.17}\text{O}_{3-\delta}$) at $T \geq 600$ °C, for GDC ($\text{Ce}_{0.8}\text{Gd}_{0.2}\text{O}_{1.9}$) at $T \geq 500$ °C and SNS ($\text{Sr}_{0.55}\text{Na}_{0.45}\text{SiO}_{2.775}$) at $T \geq 500$ °C) [29].

Fig. S4 shows the thermogravimetric analysis (TGA) of nominal $\text{La}_2\text{Ge}_{0.5}\text{Cr}_{0.5}\text{MgO}_{6-\delta}$ obtained in air and 5% H_2/N_2 flow. The curves display the loss of adsorbed $\text{H}_2\text{O}/\text{CO}_2$ between 225 and 400 °C in oxidizing atmosphere, and also oxygen between 300 and 800 °C in reducing atmosphere. In oxidizing conditions, we observed an oxidation step of the sample above 620 °C that is due to the oxidation of Cr^{3+} to Cr^{4+} . The difference in the weight loss between the TGA runs in air and in 5% H_2/N_2 clearly shows the presence of Cr^{4+} in a sample prepared at 1350 °C and slow-cooled in air, as well as the possibility of eliminating the oxidation of the Cr^{3+} by reducing the electrolyte at or above 800 °C and retaining the reducing atmosphere to below 620 °C. Upon cooling, there is little change in the weight from the high-temperature value in either atmosphere. A $T_{\text{op}} < 600$ °C would prevent oxidation of Cr^{3+} in an operating SOFC. However, the red color of our sample indicates the 3d electrons on the $\text{Cr}^{4+}/\text{Cr}^{3+}$ couples are localized; the polaronic contribution to the conductivity is, therefore expected to be small. In order to show the performance of the electrolyte containing a small Cr^{4+} concentration, we have used the electrolyte disk/pellets as-sintered at 1400 °C. We also characterized the samples after TGA up to 900 °C in air and 5% H_2/N_2 by XRD. Rietveld refined powder XRD profiles of the samples after TGA are shown in Fig. S5 at the Supporting Information. The compound remained in the perovskite R3 structure and no impurity phases were detected, which confirms the stability of the material in a reducing as well as an oxidizing environment.

Thermal expansion (dilatometry)

In order to determine the applicability of the electrolyte in a SOFC, the mechanical compatibility of the electrolyte with other SOFC components was determined: a dilatometric analysis was performed between 35 and 900 °C for several cycles; the data were only recorded during the heating runs. Fig. 7 shows no abrupt changes in the thermal expansion of $\text{La}_2\text{Ge}_{0.5}\text{Cr}_{0.5}\text{MgO}_{6-\delta}$ in all the temperature range under measurement. The thermal expansion coefficient (TEC) measured under air and 5% H_2/N_2 atmospheres between 100 and 900 °C are $11.3 \times 10^{-6} \text{ K}^{-1}$ and $11.1 \times 10^{-6} \text{ C}^{-1}$, respectively. Similar values for both electrolyte and electrode components are critical to avoid cracking problems during the start-up/shut-down cycles and the SOFC operation. These values match well with the values usually displayed by SOFC electrodes and other electrolytes (e.g. for LSGM, $\text{TEC} = 11.6 \times 10^{-6} \text{ C}^{-1}$) [52,53]. The chemical compatibility of $\text{La}_2\text{Ge}_{0.5}\text{Cr}_{0.5}\text{MgO}_{6-\delta}$ with a $\text{SrCo}_{0.8}\text{Fe}_{0.2}\text{O}_{3-\delta}$ cathode was checked by firing (1:1) mixtures of the powdered materials at 600 °C in air for 24 h; the inset of Fig. 7 shows a Rietveld analysis of the products consisting of a mixture of the unaltered phases.

Test SOFC

The performance of $\text{La}_2\text{Ge}_{0.5}\text{Cr}_{0.5}\text{MgO}_{6-\delta}$ as an electrolyte was tested in single cells in a 300-μm-thick electrolyte-supported configuration. Fig. 8 illustrates the cell voltage

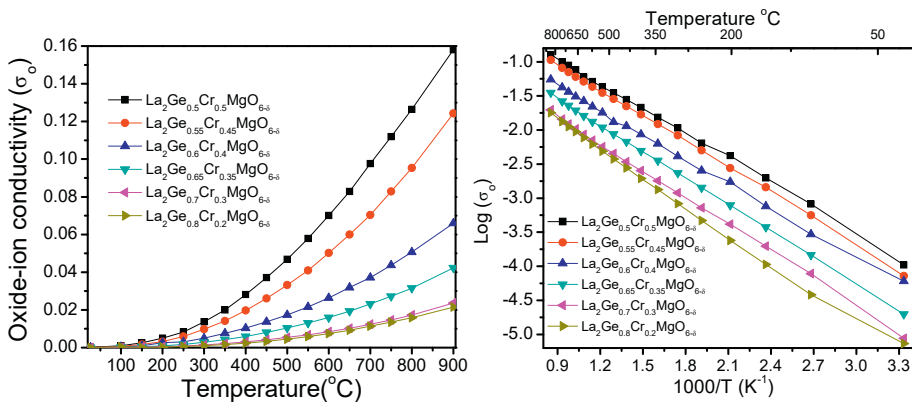


Fig. 6 – (a) Oxide-ion plus polaronic conductivity (σ_0 vs temperature (°C); (b) Arrhenius (Log σ_0 vs $1000/T$ (K⁻¹) plot for $\text{La}_2\text{Ge}_{1-x}\text{Cr}_x\text{MgO}_{6-\delta}$.

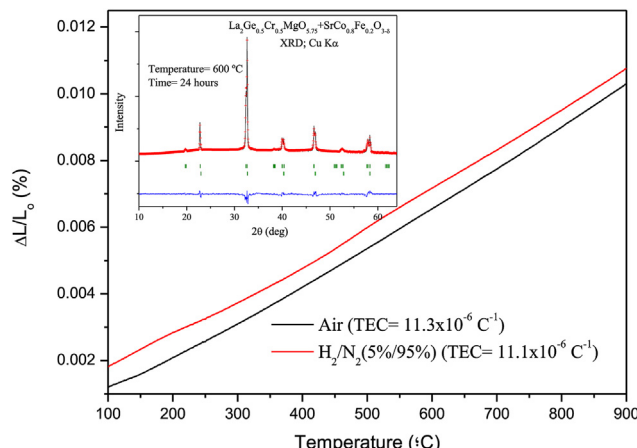


Fig. 7 – Thermal expansion determined by dilatometry of the $\text{La}_2\text{Ge}_{0.5}\text{Cr}_{0.5}\text{MgO}_{6-\delta}$. The inset shows the Rietveld-refined XRD profiles of a mixture of unaltered $\text{La}_2\text{Ge}_{0.5}\text{Cr}_{0.5}\text{MgO}_{6-\delta}$ and $\text{SrCo}_{0.2}\text{Fe}_{0.2}\text{O}_{3-\delta}$ after a thermal treatment at 600 °C in air, showing no reaction products.

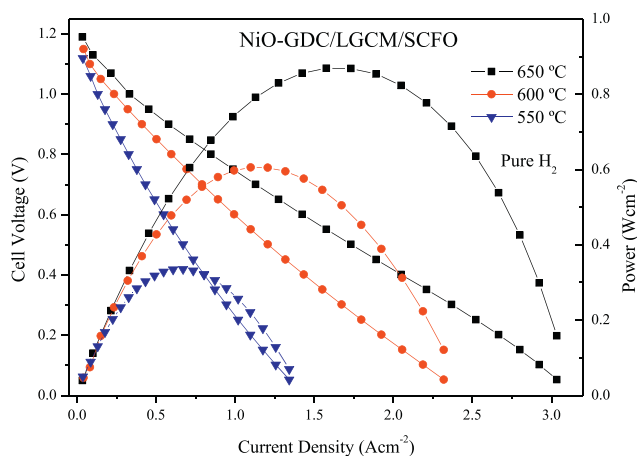


Fig. 8 – Cell voltage (left axis) and power density (right axis) as a function of the current density for the test cell with the configuration Ni-GDC/ $\text{La}_2\text{Ge}_{0.5}\text{Cr}_{0.5}\text{MgO}_{6-\delta}$ (LGCM)/SCFO in pure H_2 measured at $T_{\text{op}} = 550, 600$ and 650 °C.

and power density as a function of current density at 550, 600 and 650 °C for single cells fed with pure H_2 with a NiO-GDC anode. The maximum power densities generated by the cell are 336, 606 and 869 mW cm⁻², respectively. The peak power density of 606 mW cm⁻² obtained at 600 °C with $\text{La}_2\text{Ge}_{0.5}\text{Cr}_{0.5}\text{MgO}_{6-\delta}$ is impressive; it overcomes the best peak power densities of 431 mW cm⁻² at 600 °C for a 294-μm-thick $\text{Sr}_{0.55}\text{Na}_{0.45}\text{SiO}_{2.775}$ electrolyte [28,38] and for a 200-μm-thick LSGM-based SOFC, viz. 200 mW cm⁻² at 600 °C [54]. This performance represents a more than 3-fold power enhancement. The performance test at 600 °C shows the potential of achieving a low-temperature (300 °C < Top<600 °C) SOFC with several important technical application if, in particular, an efficient catalytic cathode for the oxygen reduction reaction (ORR) and oxygen evolution reaction (OER) at Top< 500 °C can be developed.

Conclusions

The double-perovskite $\text{La}_2\text{MgGe}_{0.5}\text{Cr}_{0.45}\text{O}_{6-\delta}$, studied from NPD data, illustrates the structural behavior of the $\text{La}_2\text{Ge}_{1-x}\text{Cr}_x\text{MgO}_{6-\delta}$ series. The presence of Cr distributed at random with Ge ions accounts for the presence of a conspicuous oxygen deficiency, responsible for the transport properties. BVEL maps show that the ionic transport is enabled around the smaller (Ge/Cr)O₆ octahedra, probably by a steric effect. The member with $x = 0.5$ shows a high oxide-ion conductivity $\sigma_0 > 10^{-2}$ Scm⁻¹ below 350 °C. The high oxide-ion mobility confirms the strategy of designing a perovskite containing cations stable in both octahedral and tetrahedral oxygen coordination, and the introduction of a cation with a strong octahedral-site preference to frustrate oxygen-vacancy ordering as in a brownmillerite phase. The superior performance of $\text{La}_2\text{MgGe}_{0.5}\text{Cr}_{0.45}\text{O}_{6-\delta}$ as the electrolyte of a SOFC operating at 600 °C appears to be limited by the catalytic electrodes; the perovskite cathode used may cation-exchange with the electrolyte above 600 °C. The threefold increase in power density output in the SOFC performance test at 600 °C shows the potential of achieving a low-temperature (Top ≥300 °C) $\text{La}_2\text{MgGe}_{0.5}\text{Cr}_{0.45}\text{O}_{6-\delta}$ -based SOFC with important technical applications.

Declaration of competing interest

The authors declare that they have no known competing financial interests or personal relationships that could have appeared to influence the work reported in this paper.

Acknowledgements

We thank the Spanish Ministry for Science and Innovation (MCIN/AEI/10.13039/501100011033) for funding the project number: PID2021-122477OB-I00. The authors wish to express their gratitude to SINQ supporting staff for making the facilities available for the neutron diffraction experiment.

Appendix A. Supplementary data

Supplementary data to this article can be found online at <https://doi.org/10.1016/j.ijhydene.2022.12.193>.

REFERENCES

- [1] Singh M, Zappa D, Comini E. Solid oxide fuel cell: decade of progress, future perspectives and challenges. *Int J Hydrogen Energy* 2021;46:27643–74.
- [2] Malavasi L, Fisher CAJ, Islam CMS. Oxide-ion and proton conducting electrolyte materials for clean energy applications: structural and mechanistic features. *Chem Soc Rev* 2010;39:4370–87.
- [3] Brett DJL, Atkinson A, Brandon NP, Skinner SJ. Intermediate temperature solid oxide fuel cells. *Chem Soc Rev* 2008;37:1568–78.
- [4] Jacobson AJ. Materials for solid oxide fuel cells. *Chem Mater* 2010;22:660–74.
- [5] Steele BCH, Heinzel A. Materials for fuel-cell technologies. *Nature* 2001;414:345–52.
- [6] McIntosh S, Gorte RJ. Direct hydrocarbon solid oxide fuel cells. *Chem Rev* 2004;104:4845–66.
- [7] Lanzini A, Leone P. Experimental investigation of direct internal reforming of biogas in solid oxide fuel cells. *Int J Hydrogen Energy* 2010;35:2463–76.
- [8] Dwivedi S. Solid oxide fuel cell: materials for anode, cathode and electrolyte. *Int J Hydrogen Energy* 2020;45:23988–4013.
- [9] Ni M, Leung MKH, Leung DYC. Technological development of hydrogen production by solid oxide electrolyzer cell (SOEC). *Int J Hydrogen Energy* 2008;33:2337–54.
- [10] Brisse A, Schefold J, Zahid M. High temperature water electrolysis in solid oxide cells. *Int J Hydrogen Energy* 2008;33:5375–82.
- [11] Herring JS, O'Brien JE, Stoots CM, Hartvigsen JJ, Shahnam M. Progress in high-temperature electrolysis for hydrogen production using planar SOFC technology. *Int J Hydrogen Energy* 2007;32:440–50.
- [12] Bernadet L, Moncasi C, Torrell M, Tarancón A. High-performing electrolyte-supported symmetrical solid oxide electrolysis cells operating under steam electrolysis and co-electrolysis modes. *Int J Hydrogen Energy* 2020;45:14208–17.
- [13] Xu N, Li X, Zhao X, Goodenough JB, Huang K. A novel solid oxide redox flow battery for grid energy storage. *Energy Environ Sci* 2011;4:4942–6.
- [14] Surya Prakash GK, Viva FA, Olah GA. Electrochemical reduction of CO₂ over Sn-Nafion coated electrode for a fuel-cell-like device. *J Power Sources* 2013;223:68–73.
- [15] da Silva FS, de Souza TM. Novel materials for solid oxide fuel cell technologies: a literature review. *Int J Hydrogen Energy* 2017;42:26020–36.
- [16] Matsuzaki Y, Yasuda I. Electrochemical properties of reduced-temperature SOFCs with mixed ionic-electronic conductors in electrodes and/or interlayers. *Solid State Ionics* 2002;152:463–8.
- [17] Athanassiou C, Pekridis G, Kaklidis N, Kalimeri K, Vartzoka S, Marnellos G. Hydrogen production in solid electrolyte membrane reactors. *Int J Hydrogen Energy* 2007;32:38–54.
- [18] Aguadero A, Fawcett L, Taub S, Woolley R, Wu K, Xu N, et al. Materials development for intermediate-temperature solid oxide electrochemical devices. *J Mater Sci* 2012;47:3925–48.
- [19] Zhao Y, Xia C, Jia L, Yu J, Li Y. Recent progress on solid oxide fuel cell: lowering temperature and utilizing non-hydrogen fuels. *Int J Hydrogen Energy* 2013;38:16498–517.
- [20] Huang J, Xie F, Wang C, Mao Z. Development of solid oxide fuel cell materials for intermediate-to-low temperature operation. *Int J Hydrogen Energy* 2012;37:877–83.
- [21] Wachsman ED, Lee KT. Lowering the temperature of solid oxide fuel cells. *Science* 2011;334:935–9.
- [22] Goodenough JB. Oxide-ion electrolytes. *Annu Rev Mater Res* 2003;33:91–128.
- [23] Ishihara T, Matsuda H, Takita Y. Doped LaGaO₃ perovskite type oxide as a new oxide ionic conductor. *J Am Chem Soc* 1994;116:3801–3.
- [24] Feng M, Goodenough JB. A superior oxide-ion electrolyte. *Eur J Solid State Inorg Chem* 1994;31:663–72.
- [25] Hideaki I, Hiroaki T. Ceria-based solid electrolytes. *Solid State Ionics* 1996;83:1–16.
- [26] Kuang X, Green MA, Niu H, Zajdel P, Dickinson C, Claridge JB, et al. Interstitial oxide ion conductivity in the layered tetrahedral network melilite structure. *Nat Mater* 2008;7:498–504.
- [27] Raj ES, Skinner SJ, Kilner JA. Electrical conductivity, oxygen diffusion and surface exchange studies on a melilite-type La_{1.05} Sr_{0.95} Ga₃O_{7+δ}. *Solid State Ionics* 2005;176:1097–101.
- [28] (a) Singh P, Goodenough JB. Sr_{1-x}K_xSi_{1-y}Ge_yO_{3-0.5x}: a new family of superior oxide-ion conductors. *Energy Environ Sci* 2012;5:9626–31.
(b) Singh P, Goodenough JB. Monoclinic Sr_{1-x}Na_xSiO_{3-0.5x}: new superior oxide ion electrolytes. *J Am Chem Soc* 2013;135:10149–54.
- [29] Wei T, Singh P, Gong Y, Goodenough JB, Huang K. Sr_{3-3x}Na_{3x}SiO_{9-1.5x} (x=0.45) as a superior solid oxide-ion electrolyte for intermediate-temperature solid oxide fuel cell. *Energy Environ Sci* 2014. <https://doi.org/10.1039/C3EE43730B>.
- [30] Nakayama S, Kageyama T, Aono H, Sadaoka Y. Ionic conductivity of lanthanoid silicates, Ln₁₀(SiO₄)₆O₃ (Ln = La, Nd, Sm, Gd, Dy, Y, Ho, Er and Yb). *J Mater Chem* 1995;5:1801–5.
- [31] Tao S, Irvine JTS. Preparation and characterization of apatite-type lanthanum silicates by a sol-gel process. *Mater Res Bull* 2001;36:1245–58.
- [32] Tolchard JR, Saiful-Islam M, Slater PR. Defect chemistry and oxygen ion migration in the apatite-type materials La_{9.33}Si₆O₂₆ and La₈Sr₂Si₆O₂₆. *J Mater Chem* 2003;13:1956–61.
- [33] Leon-Reina L, Losilla ER, Martinez-Lara M, Bruque S, Aranda MAG. Interstitial oxygen conduction in lanthanum oxyapatite electrolytes. *J Mater Chem* 2004;14:1142–9.

- [34] Leon-Reina L, Losilla ER, Martínez-Lara M, Carmen Martín-Sedeno M, Bruque S, Núñez P, et al. High oxide ion conductivity in Al-doped germanium oxyapatite. *Chem Mater* 2005;17:596–600.
- [35] Arikawa H, Nishiguchi H, Ishihara T, Takita Y. Oxide ion conductivity in Sr-doped $\text{La}_{10}\text{Ge}_6\text{O}_{27}$ apatite oxide. *Solid State Ionics* 2000;136:31–7.
- [36] Esaka T, Mina-ai T, Iwahara H. Oxide ion conduction in the solid solution based on the scheelite-type oxide PbWO_4 . *Solid State Ionics* 1992;57:319–25.
- [37] Lacerda M, Irvine JTS, Glasser FP, West AR. High oxide ion conductivity in $\text{Ca}_{12}\text{Al}_{14}\text{O}_{33}$. *Nature* 1988;332:525–6.
- [38] Martínez-Coronado R, Singh P, Alonso-Alonso J, Goodenough JB. Structural investigation of the oxide-ion electrolyte with SrMO_3 ($M = \text{Si}/\text{Ge}$) structure. *J Mater Chem* 2014. <https://doi.org/10.1039/C3TA15309F>.
- [39] Wei L, Zhang J, Yu F, Yang N, Liu S. A novel fabrication of yttria-stabilized-zirconia dense electrolyte for solid oxide fuel cells by 3D printing technique. *Int J Hydrogen Energy* 2019;44:6182–91.
- [40] Hao S-J, Wang C, Liu T-L, Mao Z-Q, Wang J-L. Fabrication of nanoscale yttria stabilized zirconia for solid oxide fuel cell. *Int J Hydrogen Energy* 2017;42:29949–59.
- [41] Murutoglu M, Ucun T, Ulasan O, Tur YK, Yilmaz H. Cold sintering-assisted densification of GDC electrolytes for SOFC applications. *Int J Hydrogen Energy* 2022;47:19772–9.
- [42] Babar ZUD, Hanif MB, Gao J-T, Li C-J, Li C-X. Sintering behavior of $\text{BaCe}_{0.7}\text{Zr}_{0.1}\text{Y}_{0.2}\text{O}_{3-\delta}$ electrolyte at 1150 °C with the utilization of CuO and Bi₂O₃ as sintering aids and its electrical performance. *Int J Hydrogen Energy* 2022;47:7403–14.
- [43] Temluxame P, Puengjinda P, Peng-ont S, Sornchamni T, Kim-Lohsoontorn P. Comparison of ceria and zirconia based electrolytes for solid oxide electrolysis cells. *Int J Hydrogen Energy* 2021;46:24568–80.
- [44] Glisenti A, Bedon A, Carollo G, Savaniu C, Irvine JTS. Reversible, all-perovskite SOFCs based on La, Sr gallates. *Int J Hydrogen Energy* 2002;45:29155–65.
- [45] Swaffer M, Slater PR, Gover RKB, Matsumura T, Kanno R, Kamiyama T. $\text{La}_2\text{MgGeO}_6$: a novel Ge based perovskite synthesised under ambient pressure. *Chem Commun* 2002;1776–7.
- [46] Lu Y, López CA, Wang J, Ch JA. Insight into the structure and functional application of Mg-doped $\text{Na}_0.5\text{Bi}_0.5\text{TiO}_3$ electrolyte for solid oxide fuel cells. *J Alloys Compd* 2018;752:213–9.
- [47] Gong Y, Sun CW, Huang Q-A, Alonso JA, Fernández-Díaz MT, Chen L. Dynamic octahedral breathing in oxygen-deficient $\text{Ba}_{0.9}\text{Co}_{0.7}\text{Fe}_{0.2}\text{Nb}_{0.1}\text{O}_{3-\delta}$ perovskite performing as a cathode in intermediate-temperature SOFC. *Inorg Chem* 2016;55:3091–7.
- [48] Wang J, Sun C-W, Gong Y-D, Zhang H-R, Alonso JA, Fernández-Díaz MT, et al. Imaging the diffusion pathway of Al^{3+} ion in NASICON-type $(\text{Al}_{0.2}\text{Zr}_{0.8})_{20/19}\text{Nb}(\text{PO}_4)_3$ as electrolyte for rechargeable solid-state Al batteries. *Chin Phys B* 2018;27:128201.
- [49] Sun C-W, Chen L, Shi S, Reeb B, López CA, Alonso JA, et al. Visualization of the diffusion pathway of protons in $(\text{NH}_4)_2\text{Si}_{0.5}\text{Ti}_{0.5}\text{P}_4\text{O}_{13}$ as an electrolyte for intermediate-temperature fuel cells. *Inorg Chem* 2018;57:676–80.
- [50] Sun CW, Lopez CA, Antonio Alonso JA. Elucidating the diffusion pathway of protons in ammonium polyphosphate: a potential electrolyte for intermediate temperature fuel cells. *J Mater Chem* 2017;5:7839.
- [51] Brown ID. Recent developments in the methods and applications of the bond valence model. *Chem Rev* 2009;109:6858–919.
- [52] Hayashi H, Suzuki M, Inaba H. Thermal expansion of Sr- and Mg-doped LaGaO_3 . *Solid State Ionics* 2000;128:131–9.
- [53] Petric A, Huang P, Tietz F. Evaluation of La–Sr–Co–Fe–O perovskites for solid oxide fuel cells and gas separation membranes. *Solid State Ionics* 2000;135:719–25.
- [54] Wan J-H, Yan J-Q, Goodenough JB. LSGM-based solid oxide fuel cell with 1.4W/cm^2 power density and 30 day long-term stability. *J Electrochem Soc* 2005;152:A1511–5.